RSC Advances

Fluorescent carbon quantum dots, capacitance and catalysis active porous carbon microspheres from beer

Journal:	*RSC Advances*
Manuscript ID:	RA-ART-03-2015-005365.R1
Article Type:	Paper
Date Submitted by the Author:	03-May-2015
Complete List of Authors:	gao, zhiyong; henan normal university, College of Chemistry and Environmental Science Wang, Xiaorui; Henan Normal University, Chang, Jiuli; Henan Normal University, College of Chemistry and Environmental Science Wu, Dapeng; henan normal university, Wang, Lan; Henan Normal University, Liu, Xiao; henan normal university, Xu, Fang; henan normal university, Guo, yuming; henan normal university, Jiang, kai; henan normal university, School of chemistry and chemical engineering

Cite this: DOI: 10.1039/c0xx00000x

www.rsc.org/xxxxxx

Fluorescent carbon quantum dots, capacitance and catalysis active porous carbon microspheres from beer

Zhiyong Gao, Xiaorui Wang, Jiuli Chang, Dapeng Wu, Lan Wang, Xiao Liu, Fang Xu, Yuming Guo, Kai Jiang[*]

Received (in XXX, XXX) Xth XXXXXXXXX 20XX, Accepted Xth XXXXXXXXX 20XX
DOI: 10.1039/b000000x

Fluorescent nitrogen containing carbon quantum dots (NCQDs) and porous carbon microspheres (PCMs) were simultaneously synthesized by a facile hydrothermal method using beer as precursor. The afforded NCQDs in supernatant exhibited strong blue fluorescence in aqueous solution and dry state under UV light excitation, showing the huge potential as fluorescent dye. The PCMs in sediment showed great potential in supercapacitor electrode and catalyst for certain reaction. After $ZnCl_2$ activation at 900 ^{o}C, the obtained highly porous a-PCM$_{900}$ (denoted according to activation temperature) offered a high specific capacitance of 273.2 F g^{-1} at 1 A g^{-1}, excellent rate capability and cycling stability when employed as supercapacitor electrode. Moreover, a-PCM$_{900}$ could also serve as efficient non-noble metal catalyst for reduction conversion of 4-nitrophenol to 4-aminophenol by $NaBH_4$ with high activity and well reusability.

Introduction

Carbon is an extremely intriguing element in material realm. Due to the different electron orbital types (e.g. sp, sp^2 or sp^3 hybrid) and dimension dependent electric and surface properties, carbon materials, in form of fullerene, carbon nanotube, graphene, graphdiyne, etc have shown giant potential in a myriad of applications including nanoelectronics,[1,2] catalyst supports,[3] sensors,[4] drug delivery[5] and electrochemical energy storage.[6,7] Among the various carbon materials, fluorescent carbon quantum dots (CQDs) emerge as a rising star for the tunable photoluminescence (PL), high resistance to photobleaching, low cytotoxicity, and robust chemical inertness relative to traditional heavy metal chalcogenides quantum dots and organic fluorescent dyes.[8,9] Therefore, CQDs have attracted tremendous research interests in last decade motivated by the applications in bioimaging,[10] photocatalysis,[11,12] fluorescent sensors[13,14] and light emitting diodes.[15,16] Generally, the PL performance of CQDs with solely carbon framework is relatively low, heteroatoms (N and/or S, P) incorporation have proven to be a useful approach to improve the electronic structure, surface property and therefore fluorescence emission by introducing an upward shift of Fermi level and surface energy trap sites. Hence, heteroatoms incorporated CQDs with tunable PL performances were intensively investigated for pursuit of desired application performances.[17,18]

On the other hand, heteroatoms containing porous carbons represent a big class of fascinating materials with great potential in surface and conductivity related applications such as supercapacitor electrodes and catalysts for certain reactions as a consequence of the outstanding surface areas, high conductivities of carbon framework and the abundant active sites by heteroatoms doping.[19,20] As for supercapacitor electrodes, the porous and carbonized texture is essential for a high ions accessible surface area and electrons conductivity. Additionally, heteroatoms doping can supply extra pseudo-capacitance and wettability to electrolyte, thereby enhancing the overall capacitance, rate performance and cycling stability.[21,22] Heterogeneous catalysts share the same structural and interfacial characteristics with supercapacitor electrodes, high surface area and conductivity are also highly required for sufficient contact with reactants and efficient charge transferring, and the doped heteroatoms with different electronegativities can further improve the polarity of adjacent skeletal carbon atoms, thus creates rich catalytically active sites and promotes the catalytic activities on some redox reactions.[23,24]

Given the excellent usage of NCQDs and heteroatoms doped porous carbons, it is critical to develop efficient and cost effective strategies for simultaneous synthesizing of NCQDs and PCMs in a green manner to make the best of these materials. Currently, the preparation of heteroatoms doped carbon materials mainly includes two pathways, the post treatment of carbon framework with reactive heteroatoms modifiers and direct pyrolysis of carbon and heteroatoms containing precursors.[19] Among the various methods for doped carbons preparation, hydrothermal carbonization is accepted as the most efficient one owing to the simple equipment, easy manipulation and nontoxic synthesis procedure. For hydrothermal synthesis of carbon materials, an appropriate precursor is another premise, the carbon and hetero-element containing precursors are considered to be ideal candidates for NCQDs and PCMs preparation.

Due to the comprising of carbon and hetero-elements containing nutriment gradients, nontoxicity, easy availability and sustainable resource, natural feedstocks are ideal precursors for heteroatoms doped carbons with outstanding cost advantage and environmental safety. Various natural feedstocks such as fruits juice,[25,26] vegetations[27,28] and food related semi-manufactured products[29,30] were widely employed as precursors for preparation of NCQDs and PCMs. Beer is a widely consumed beverage in our daily diet. The containing of rich saccharides and amino acids makes beer a promising precursor for preparation of nitrogen incorporated carbons. Herein, beer was tried as precursor for hydrothermal synthesis of carbon materials for the first time. As expected, both NCQDS and PCMs can be formed simultaneously, which can be easily separated by centrifugation. The highly fluorescent NCQDs exhibit strong fluorescence in both solution and dry state, showing the potential in fluorescent antifake labeling and information encryption. PCMs in the sediment demonstrate porous texture, $ZnCl_2$ activation treatment substantially improves the electrochemical performance as supercapacitor electrode and catalytic activity on 4-nitrophenol reduction.

Experimental

Samples preparation

Fluorescent NCQDs and PCM were synthesized by a facile hydrothermal treatment of beer (Hangkong Beer, Xinxiang, China). In brief, 80 mL of commercial beer was initially stirred for 20 min to remove the dissolved carbon dioxide bubbles. Subsequently, the beer solution was transferred into a Teflon-lined autoclave and subjected to hydrothermal treatment at 200 ^{o}C for 20 h. After being cooled down naturally, orange supernatant (CQDs) and dark sediment (PCM) were produced. The PCM precipitate was centrifuged and washed repeatedly with deionized water and dried at 60 ^{o}C. For chemical activation treatment, PCM was dispersed in $ZnCl_2$ aqueous solution with PCM/$ZnCl_2$ mass ratio of 1:3 and stirred overnight, the homogeneous mixture was then dried at 80 ^{o}C to form thick slurry, which was subjected to calcination at a heating rate of 5 ^{o}C min^{-1} to 600, 700, 800 or 900 ^{o}C and maintained at these temperatures for 2 h under nitrogen atmosphere. After being cooled down, the products were rinsed thoroughly with 2 M HCl aqueous solution to get rid of any metal residues and washed copiously with deionized water. The afforded a-PCMs were denoted as a-PCM$_{600}$, a-PCM$_{700}$, a-PCM$_{800}$, or a-PCM$_{900}$, respectively according to activation temperature.

Characterizations

UV-Vis absorption and fluorescence emission spectra of the NCQDs aqueous solution were recorded on TU-1900 UV-vis spectrophotometer (Purkinje, Beijing, China) and JASCO FP-6500 fluorescence spectrophotometer. The fluorescence quantum yield (QY) was estimated according to the relative integrated area of NCQDs emission peak and absorbance intensity using quinine sulfate as reference.[31] ^{13}C-nuclear magnetic resonance spectrum (^{13}C-NMR) of NCQDs dispersed in dimethyl sulfoxide-d6 (DMSO-d6) was recorded on a 400 MHz NMR spectrometer (Bruker AV400).

The morphological and microstructural analyses of PCM and a-PCMs were performed by scanning electron microscopy (SEM, JEOL JSM-6390), high resolution transmission electronic microscopy (HRTEM, JEOL JEM-2100), X-ray powder diffraction (XRD, Bruker D diffractometer with Cu Ka radiation), Fourier transform infrared spectroscopy (FTIR, Bio-Rad FTS-40) and X-ray photoelectron spectroscopy (XPS, ThermalFisher ESCALab 250 X-ray photoelectron spectrometer with Al Ka radiation). Nitrogen adsorption-desorption isotherms were measured on a Micromeritics Gemini 2380 surface area analyzer at 77 K. The specific surface areas and pore size distributions of the samples were calculated using multiple points Brunauer-Emmett-Teller (BET) and Barrett-Joyner-Halenda (BJH) methods. The wettabilities of PCMs and a-PCMs were compared by water contact angle measurements, a droplet of vertically dangled water (6 μL) was slowly contacted with the surface of PCMs or a-PCMs based supercapacitor electrode, and the contact angles were recorded 5 s after the placement of droplet onto electrode surface.

Electrochemical properties

The PCM and a-PCMs based supercapacitor electrodes were fabricated by spreading of slurry contains 85 mw% active material, 10 mw% acetylene black and 5 mw% polytetrafluoroethylene binder onto clean stainless steel collector, of which the dosage of active material onto each collector is about 1 mg. The symmetric supercapacitors were assembled by sandwiching of a hydrophilic separator between two identical electrodes (active area of 1 cm^{2}), followed by immersing in 1 M H_2SO_4 electrolyte. Electrochemical parameters including cycling voltammogram (CV), galvanostatic charging-discharging curve (GCD) and electrochemical impedance spectrum (EIS) of the symmetric supercapacitors were all measured in double-electrode configuration. CVs of the supercapacitors were recorded on a CHI 660D workstation (Chenhua, Shanghai) over potential range of -1~1 V at scan rates of 10-500 mV s^{-1}. GCDs of the symmetrical supercapacitors were measured on a Land CT2001A cell test system (Wuhan, China). EIS measurements were also measured on CHI 660D workstation, the impedances were recorded over the frequency range of 10^{5}~0.01 Hz at open circuit potential with an ac perturbation of 5 mV. The specific capacitances (C_ss, F g^{-1}) of the electrode materials were calculated from GCD measurements according to the following Eq:

$$C_s = I\Delta t/(\Delta V\times m) \qquad \text{(Eq. 1)}$$

Where I (A) represents the discharge current, ΔV (V) is the potential change within the discharge duration Δt (s), m (g) is the total mass of active material on each electrode, the active materials were weighted accurately for C_s calculation.

Catalytic reduction of 4-nitrophenol

The catalytic activities of a-PCMs were evaluated using a typical model of 4-nitrophenol reduction by $NaBH_4$ at ambient temperature. Typically, 5 mL of 4-nitrophenol aqueous solution (1 mM) was added to 20 mL of newly prepared $NaBH_4$ solution (1 mg mL^{-1}) to form a homogeneous reaction mixture with the molar ratio of 4-nitrophenol:$NaBH_4$ to be 1:100. Subsequently, 0.6 mg of catalyst was added to the mixture under vigorous stirring to initiate the reaction. During the reaction process, 2 mL of reaction solution was sampled at a regular time interval and filtered immediately to monitor the time dependent UV-vis spectroscopy variation. The reaction rate was monitored according to the gradual decrease in characteristic absorbance of 4-nitrophenolate ions at 400 nm. The concentration ratio of 4-nitrophenol at time t to initial time 0, C_t/C_0 can be expressed as A_t/A_0 according to Lambert-Beer's law. The reaction kinetics of a-PCM$_{900}$ catalyst was fitted by $-dC_t/dt = kC_t$ or $\ln(C_t/C_0) = -kt$. In the cycling experiment of a-PCM$_{900}$ catalyst, the remnant catalyst from reaction system was washed thoroughly with deionized water and reused in the following cycle of catalytic reaction.

Results and discussion

Formation process toward NCQDs and PCMs

Fig. 1 The schematic of formation process for NCQDs and PCMs.

Beer is a popular beverage contains rich nutritional ingredients including maltose, amino acid, glutathione, vitamins and ethanol. These carbon and nitrogen containing organics make beer a good candidate as precursor for preparation of N-containing carbon materials. At hydrothermal temperature, the aggregation of reactive radical intermediates derived from dehydroxylation, dehydrogenation, as well as cleaving and rearrangement of ether rings in maltose leads to large aromatic carbon framework.[32-34] Meanwhile, the nucleophilic attacking of amino acids or glutathione onto carbon framework introduces N and S elements, thus produces O, N and S containing carbonaceous materials. Undergoes hydrothermal reaction at 200 ^{o}C for 20 h, the pale yellow beer solution transforms into orange NCQDs supernatant and a rather high yield of dark PCM sediment (Fig. 1), intuitively evidences the carbonization of beer. Shortening of reaction duration results in obviously lower yield of sediment whereas similar color of supernatant, implies the lower conversion ratio toward PCM. Given the same precursor and reaction condition, it is presumably that the formation of NCQDs and PCM experience similar intermediates. During hydrothermal process, the polymerization of reactive intermediates forms NCQDs colloid with small size. Further aggregation of larger intermediates produces PCM with much larger size. Direct hydrothermal treatment of NCQDs for 20 h results in the fading in supernatant color and the formation of carbon microspheres (Fig. S1), manifests that NCQDs are also intermediates or building block toward PCMs, hence the high yield of PCM at prolonged hydrothermal reaction time is reasonable. From this viewpoint, the yield of NCQDs and PCMs can be readily tuned by altering reaction duration.

Characterizations and PL properties of NCQDs

By centrifugation, NCQDs was obtained in supernatant. Fig. 2a presents the TEM image of NCQDs, it can be observed that NCQDs show dark dots with uniform size of *ca*. 6 nm and well dispersity, indicating the efficient formation of NCQDs. HRTEM image (Fig. 2b) of NCQDs displays low contrast against the background, which is typical for carbonaceous material owing to the low atomic weight and tiny size. Ambiguous but identifiable lattice fringes appear in NCQDs, indicates the periodic arrangement of lattice points inside NCQDs. The lattice spacing is measured to be 0.21 nm, which corresponds to (101) facet of planar hexagonal lattice in graphitic carbon, suggesting the formation of graphitized micro regions in NCQDs. SAED pattern (inset) of NCQDs displays ambiguous diffraction rings, suggests the largely amorphous phase of NCQDs. EDS analysis shows the containing of C, O, N and trace amount of S elements in NCQDs (Fig. S2), verifying the successful doping of N and S atoms.

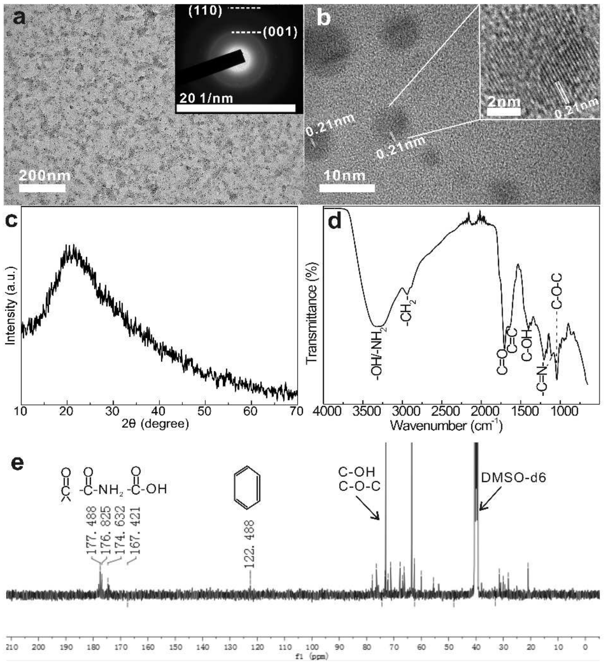

Fig. 2 (a) TEM and SAED (inset), (b) HRTEM, (c) XRD, (d) FTIR and (e) ^{13}C-NMR spectra of NCQDs.

XRD pattern of NCQDs (Fig. 2c) shows a broad peak at 21 ^{o}, which corresponds to the reflection of (002) plane with an interlayer spacing of 0.45 nm. The broad diffraction peak reveals the amorphous phase of NCQDs, which coincides with the SAED result, the larger interlayer spacing relative to graphite is mainly ascribed to the less effective π-π stacking interaction owing to the rich intrastratal defects and the existence of abundant surface functional groups around NCQDs.[35,36] The structural feature of NCQDs was further characterized by FTIR, as shown in Fig. 2d, the strong band located at 3437 cm^{-1} indicates the presence of rich -OH and -NH$_2$ groups.[37,38] Two weak peaks at 2940 and 1369 cm^{-1} are attributed to the stretching and bending vibrations of C-H bonds.[37,38] The strong peaks at 1707 and 1647 cm^{-1} evidence the presence of carbonyl and amide groups in NCQDs.[38] The peak at 1410 cm^{-1} is attributed to the tertiary C-OH stretching vibrations.[39] Moreover, another two strong peaks located at 1250 and 1020 are attributed to the C=N/C-N vibration and C-O-C bonds.[37,40] All of these vibration peaks indicate the presences of hydroxyl, carbonyl, amide, aromatic ether groups in NCQDs. ^{13}C-NMR spectrum of CQDs includes a groups of peaks located at chemical shift of 167~177 ppm, which are attributed to the C=O bonds in amide, carbonyl and carboxyl groups. The weak band at 122 ppm corresponds to the aromatic C=C rings in carbon skeleton. The strong peaks located in the range of 50~80 ppm are mainly caused by the alcohol and ether groups,[38] all of these characteristic peaks coincide with the FTIR and HRTEM results, further evidences the presence of carbonyl carbonxyl, amide, alcohol and ether groups on graphene-like aromatic carbon framework, all of these polar or hydrophilic groups result in charged surface (Fig. S3) of NCQDs colloid and therefore well dispersity in aqueous media.

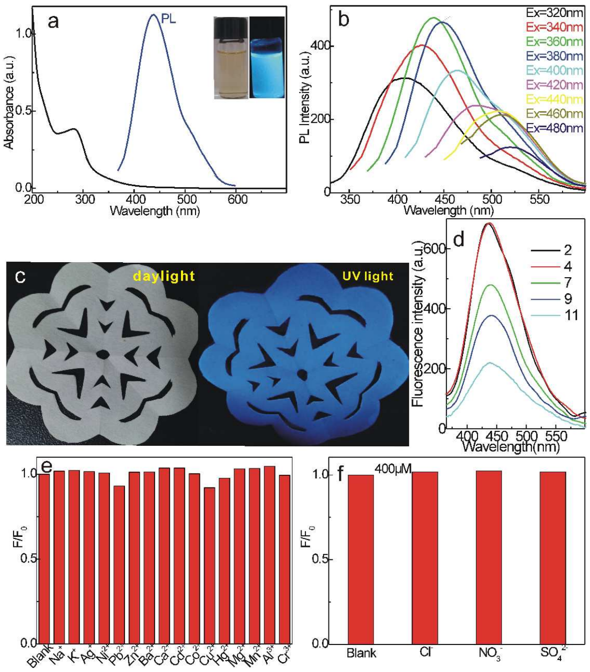

Fig. 3 (a) UV-vis absorption and fluorescence (E_x=360 nm) spectra of diluted NCQDs solution, inset: photograph of NCQDs solution under daylight and UV lamp (365 nm). (b) Fluorescence spectra under various excitation wavelengths. (c) Digital images of NCQDs dyed filter paper clipart under daylight and UV lamp in dry state. (d) Fluorescence of NCQDs at different pH values. PL intensities of NCQDs upon addition of 400 μM of different cations (e) and anions (f).

Fig. 3a shows the UV-vis absorption and fluorescence spectra of NCQDs, the absorption spectrum (black curve) includes a peak at 280 nm, which is ascribed to the n-π^* transition of C=O/C=N groups in NCQDs.[41,42] The strong absorption below 250 nm is attributed to the C=C/C-C transition.[39] Upon excitation at 360 nm, diluted NCQDs solution demonstrates a strong PL peak centered at 430 nm (blue curve). The full width at half maximum of PL peak is *ca*. 80 nm, which to some extent attests the narrow size distribution of NCQDs. Under the irradiation of ultraviolet lamp (centered at 365 nm), the transparent NCQDs aqueous solution emits brilliant blue fluorescence (inset). Fig. 3b presents the fluorescence spectra of NCQDs excited by different incident light within 320~480 nm at interval of 20 nm, the emission peaks red shift gradually from 400 nm to 580 nm and the highest fluorescent emission achieves at 430 nm under 360 nm excitation, demonstrating excitation dependent emission color of NCQDs, which is common for most CQDs. The QY calculated indirectly based on quinine sulfate (QY=54 %) is 21 %, showing the high PL performance of the as-obtained NCQDs. The QY is apparently higher over that of CQDs synthesized using solely maltose as precursor (3 %), the emission intensities and brightness are also apparent higher than that of maltose derived CQDs (Fig. S4), suggesting the doped N and trace S atoms are the main origination of the high fluorescence of NCQDs. The doping of heteroatoms introduces new surface energy trap sites, which promotes the electrons transition and radiative recombination, therefore improves the PL performance of NCQDs.[17,42,43] When a piece of filter paper was dyed by diluted NCQDs solution and subsequently dried, the filter paper still show bright blue fluorescence under UV lamp (365 nm), suggesting the well compatibility with paper fiber and the capability of maintaining strong PL feature in dry state. Considering the colorlessness of NCQDs adsorbed on filter paper and the low elemental toxicity, NCQDs can be potentially applied in antifake labeling and information encryption techniques. The influences of acidity and inorganic ions on PL performance were also investigated. As shown in Fig. 3d, the fluorescence is strong at acid media, and decreases sharply as pH increases without altering in peak wavelength. This expectional pH dependent trend is apparently different from other CQDs, of which the maximum fluorescence is achieved at neutral or alkaline media.[17,36] The strong emission at acid condition is presumably related to the protonation of interfacial or interior chemical groups such as carbonyl, amide or C=N bonds in NCQDs, which serve as fluorophores resulting in the strong fluorescence, the deprotonation of these groups declines the PL intensity, whereas too strong acidity causes the saturation of protonated groups, therefore the PL intensity no longer increases at strong acid media. The acidity sensitive feature within pH value of 4~11 implies the likelihood of our NCQDs as pH sensitive fluorescent probe in biological and biomedical applications. The addition of different cations and anions (400 μM) only cause faint decay in emission intensity of NCQDs (Fig. 3e-f), evidencing the robust anti-interference ability in complicated chemical environments.

Morphologies, microstructures and surface properties of PCMs

Besides the fluorescent NCQDs, a high yield of PCMs was also produced simultaneously in sediment. SEM image of PCMs (Fig. 4a) shows interconnected microspheres with size of 5~10 μm, which is three orders of magnitude larger than NCQDs. TEM image (Fig. 4b) exhibits dark body of the interconnected microspheres with a high contrast against the background, which is mainly due to the large size and relatively dense interior texture of the microspheres. $ZnCl_2$ is a common activation reagent that can promote the dehydration and aromatization of carbon framework and create rich pores.[44,45] Herein, the PCM was subjected to $ZnCl_2$ activation at different temperatures, the afforded a-PCMs all exhibit highly fused microspheres (Fig. S5), the higher activation temperature even causes severe crosscutting of outer layer microspheres, which indicates the activation not only creates countless pores inside the microspheres, but causes the surface cutting of outer microspheres. From Fig. 4c, a-PCM_{900} shows interconnected microspheres, the crosscut microspheres more clearly reveal the three dimensional fusion of adjacent microspheres, which will endow the material with efficient charge propagation pathways and therefore enhanced conductivity. From TEM in Fig. 4d, the rim of microsphere exhibits semitranslucent apparence composing of alternate dark and light spots, revealing the much hollowed interior and the homogeneous embedding of micropores inside PCM with a high density, which validates the pore generating effect by $ZnCl_2$. HRTEM image of a-PCM_{900} (Fig. 4e) shows incontinuous and curl fringes, which is typical characteristics of carbon materials, showing the partial crystallization of a-PCM_{900}. The partial crystallization and the highly porous texture are essential for surface and conductivity dependent applications such as supercapacitor electrode or catalysts for both charge propagation and ions (reactants) accessibility to deep inner surface of a-PCM_{900} can be simultaneously accomplished.

Fig. 5a shows the XRD patterns of PCM and a-PCMs, a broad peak centered at 21° associating with (002) planes of graphitic

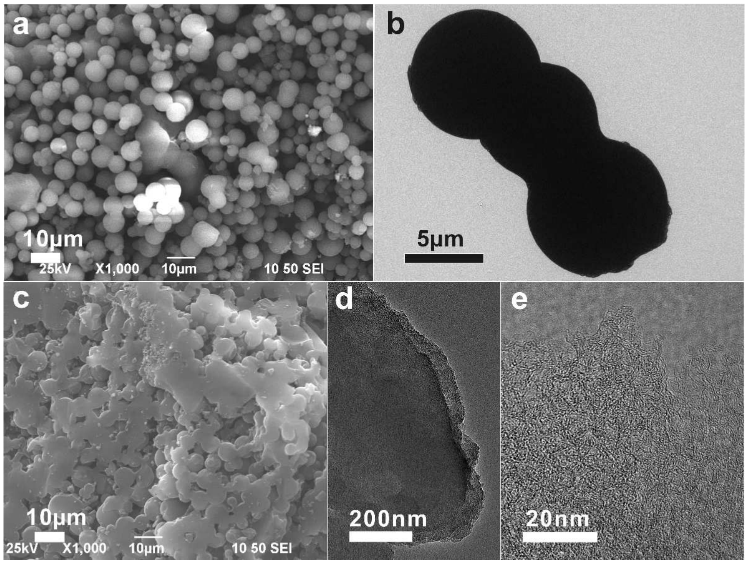

Fig. 4 (a) SEM and (b) TEM of PCM, (c) SEM, (d, e) TEM of a-PCM$_{900}$.

carbon can be observed for PCM, the low intensity and broad peak indicate the low crystallinity. After activation, the slight increase in diffraction intensity implies the enhanced crystallinity. Meanwhile, the peak position shifts to higher angle, indicating the narrowed interlayer spacing in a-PCMs, which is presumably due to the removal of functional groups or releasing of volatile substances onto both sides of graphitic carbon layers at high temperature. Additionally, another broad band at 43 ° appears, indicating the increased periodicity and therefore higher structural integrity of in-plane graphitic carbon framework, which clearly evidences the increased graphitization degree of a-PFCs. The enhanced graphitization by activation is beneficial for a higher conductivity, which is especially valuable in view of the largely amorphous nature of all samples. At low angle end, the strong diffraction baseline for a-PCM$_{600}$ and a-PCM$_{700}$ is attributed to the high density of micropores embedded in carbon framework,[46] suggesting the highly microporous texture of both samples. Whereas for a-PCM$_{800}$ and a-PCM$_{900}$, the baseline reduces, implies the decreased microporosity and therefore the higher density and conductivity.

Fig. 5b presents the FTIR spectra of PCM and a-PCMs, as for PCM, the strong peaks at 3417 cm^{-1} and 1625 cm^{-1} are attributed to the stretching and bending vibration modes of -OH/-NH$_2$ groups, another strong absorption at 1695 cm^{-1} is associated with the carbonyl vibration mode. The weak peaks at 1436 and 1253 cm^{-1} is the C-N/C=N stretching vibration absorption.[37,47] All these vibrations are similar to NCQDs except some differences in peak intensity, suggesting the similar chemical composition between PCM and NCQDs. Undergo activation treatment, the peaks intensity decreases apparently, suggesting the removal of some functional groups at high activation temperature. The strong peak at 3447 cm^{-1} indicates the generation of hydroxyl groups. The weak peaks at 1724, 1690, 1625 cm^{-1} are attributed to carboxyl, carbonyl, hydroxyl groups respectively, manifesting the containing of these polar groups in a-PCMs. The surface chemical compositions of PCM, a-PCM$_{600}$ and a-PCM$_{900}$ were further measured and compared *via* XPS analyses. From Fig. 5c, the survey spectrum of PCM (black curve) comprises three peaks with binding energy at 284.2, 532.7 and 400.2 eV, which are characteristic of C1s, O1s and N1s orbital, respectively, indicating the surface composition of PCM includes C, O and N elements. Whereas for a-PCMs, the intensities of O1s and N1s peaks decrease to different extents (red and green curve), suggesting the removal of partial N and O elements by activation treatment. Peak deconvolution analyses of C1s and N1s reveal the presence of C-C/C=C skeleton, pyridinic-, pyrrolic- and graphitic C=N, C-N/C-O-C and C=O groups in PCM (Fig. S6a-b). The activation treatment increases the fractions of C-C/C=C bonds (Fig. S6c-d), pyridinic- and graphitic-N in a-PCM$_{900}$ (Inset in Fig. 5c). As for nitrogen containing carbons, the pyridinic- and pyrrolic-N atoms can offer essential hydrophilicity, pseudocapacitance as well as enhanced catalytic activity when used as supercapacitor electrode materials and catalyst.[21,24] In addition, the enhanced fraction of graphitic N further improves the conductivity of a-PCM$_{900}$, hence enhanced capacitive and catalytic performances of a-PCM$_{900}$ are possible.

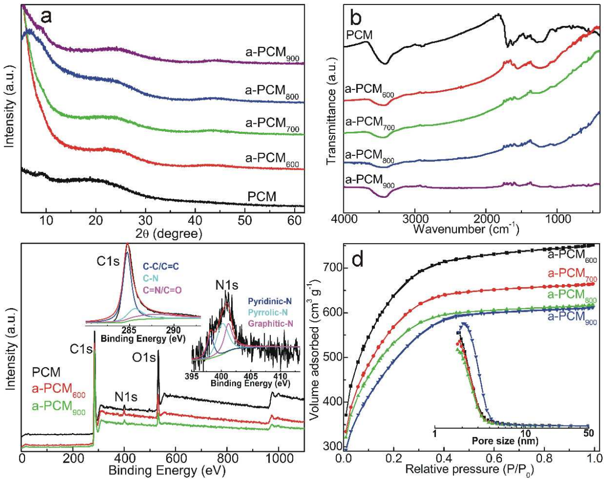

Fig. 5 (a) XRD and (b) FTIR of PCM and a-PCMs. (c) XPS survey spectra of PCM, a-PCM$_{600}$ and a-PCM$_{900}$, inset: high resolution C1s and N1s XPS spectra of a-PCM$_{900}$. (d) N_2 sorption isotherms and BJH pore size distributions of a-PCMs.

To further evaluate the porosity variation by ZnCl$_2$ activation, N_2 sorption isotherms of PCM and a-PCMs were measured. All the samples demonstrate type I (Langmuir) isotherm featured by a rapid and pronounced adsorption at low pressure and gradual saturates at higher pressure (Fig. S7 and Fig. 5d), indicating the predominantly microporous texture. Faint hysteresis loops can also be observed for PCM and a-PCM_{900}, implies the coexistence of a small fraction of mesopores within the carbon framework. BET surface areas of a-PCM_{600}, a-PCM_{700}, a-PCM_{800}, and a-PCM_{900} are 2120.7, 1917.8, 1779.5 and 1727.2 m^2 g^{-1}, respectively, all of which are more than three times higher over that of PCM (488.2 m^2 g^{-1}), highlighting the dramatic hollowing effect by activation (Table S1).[48] The gradual decline in surface area at higher activation temperature is mainly due to the heat shrinkage of carbon framework.[49] With the increment of activation temperature from 600 to 900 °C, the mesopores surface area ratios increases from 23.9 % to 29.7 %, manifests the formation of more mesopores, which may be caused by the more severe etching along the internal wall of micropores, although the overall surface area decreases concomitantly due to the crystallization and the shrinkage of texture. BJH pore size distribution of PCM show a high probability at micropores region with a side peak at mesopores range, showing the coexistence of micro- and mesopores. A-PCMs show mainly micropores, as for a-PCM_{900}, the pore size is apparently widened, indicating the higher fraction of mesopores, which can also be verified by the much lower slope at low pressure region in sorption isotherm and the faint hysteresis loop. The existence of mesopores is highly desired for application as electrode materials and catalysts, for the wider pore size allows more efficient diffusion and mass transfer of electrolyte ions or reactant molecules to access the inner surface of electrode or catalyst with less geometric hindrance, enhancing the surface utilization ratio. Moreover, the enhanced crystallinity of carbon framework and increased fraction of graphitic N provide essential conductivity for electrons propagation. Hence, a-PCM_{900} is expected to be a more suitable supercapacitor electrode material or catalyst as compared with its cousins synthesized at lower activation temperatures. The hollowed texture of a-PCMs increases the surface roughness, which is beneficial for slightly higher wettability (Fig. S8),[50] as a result, better a-PCMs/electrolyte ions (reactant) interface compatibility is achieved, which further affords more efficient capacitive and catalytic performances, albeit some polar groups are removed according to FTIR characterization (Fig. 5b).

Electrochemical performances of a-PCMs

The electrochemical performances of PCM and a-PCMs as supercapacitor electrodes were measured in symmetric double-electrode configuration within 1 M H_2SO_4 electrolyte. Fig. 6a shows the CVs of PCM and a-PCMs based supercapacitors at 50 mV s^{-1}, all of them show quasi-rectangular shape with high capacitive response superimposed with a pair of weak and reversible redox humps in potential range of -0.5~0.5 V, suggesting the predominant EDL capacitance coupled with a slight pseudocapacitance. The high EDL capacitance is mainly derived from the highly porous texture with high surface areas, whereas the pseudocapacitance may be derived from the redox transformation between different states of nitrogen and oxygen functionalities.[51,52] In comparison with PCM supercapacitor, a-PCMs devices demonstrated substantially higher plateau currents and therefore much larger loop areas, which imply the dramatically higher charge storage capacity. The activation causes substantially enlarged surface area for accumulation of electrolyte ions, thus drastically enhanced capacitance is achieved. As for the a-PCMs supercapacitors, the plateau current and therefore the loop area increases with activation temperature, which is mainly due to the more efficient ions accumulation onto deep inner surface of porous electrode as a result of the larger pore size, the higher surface utilization ratio leads to the higher capacitance.

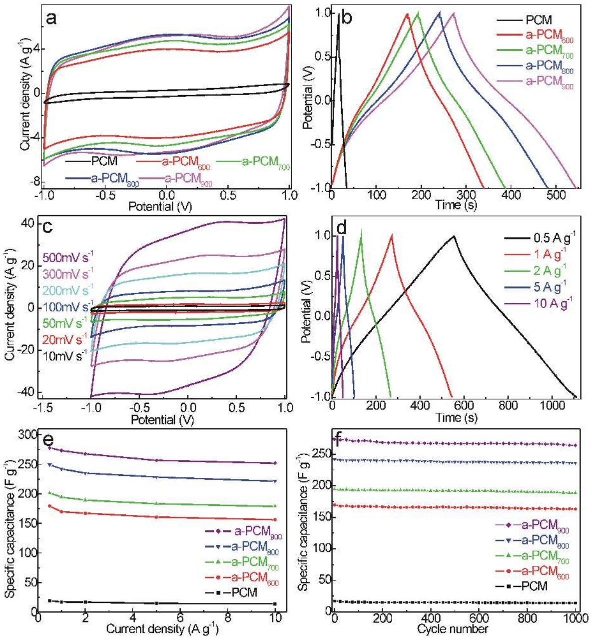

Fig. 6 (a) CVs and (b) GCDs of symmetric supercapacitors based on PCM and a-PCMs. (c) CVs of a-PCM_{900} supercapacitor at various potential scanning rates. (d) GCDs of a-PCM_{900} supercapacitor at various current densities. (e) Rate capabilities and (f) cycling stabilities of PCM and a-PCMs devices.

To further compare the capacitive behavior of PMC and a-PMCs, GCDs of PCM and a-PCMs supercapacitors were tested at 1 A g^{-1}, all the supercapacitors show symmetric charging and discharging branches with slight deviation from linear, indicating the presence of low pseudocapacitance in all samples. The almost identical charging and discharging time suggests the similar charging and discharge capacitances, namely the excellent coulombic efficiency for all supercapacitors. As compared with PCM, a-PCMs show much lower voltage drop and much longer discharge duration, indicating the lower inner resistance and the dramatically higher C_s. Amongst the a-PCMs, the discharging duration differs apparently with activation temperature. C_s values of a-PCM_{600}, a-PCM_{700}, a-PCM_{800} and a-PCM_{900} electrodes according to Eq. 1 are calculated to be 169.8, 194.4, 242.1 and 273.2 F g^{-1}, respectively at 1 A g^{-1}, suggesting a-PCM_{900} is the most efficient supercapacitor electrode material. C_s value of a-PCM_{900} is superior over or comparable to other porous carbon materials,[21,53-57] showing the potential as supercapacitor electrode. In view of the highest C_s and the lower inner resistance, the electrochemical features of a-PCM_{900} were further investigated. Fig. 6c shows CVs of a-PCM_{900} supercapacitor within potential scanning rates of 10~500 mV s^{-1}, it is clear that the capacitive current increases monotonously with scan rate, no apparent lean of CVs can be observed, and the reversible redox peaks can still be seen even at 500 mV s^{-1}, suggesting the high charge propagation ability of electrode and efficient ionic diffusion of electrolyte, both of which will further result in a high rate capability. GCD of a-PCM_{900} supercapacitor at various current densities are also shown in Fig. 6d, with the increment in current density, voltage drop slightly increases, which is mainly derived from the increased electrolyte diffusion resistance because of the overwhelming microporosity of a-PCM_{900}, the deep inner surface of micropores can not be fully utilized at higher operation current densities, resulting in the declined C_s at higher current densities. C_s of a-PCM$_{900}$ supercapacitor from discharging curves are calculated to be 277.8, 273.2, 267.7, 256.4, and 251.9 F g^{-1}, respectively at 0.5, 1, 2, 5 and 10 A g^{-1}. An impressive 90.7 % C_s retention is achieved within 0.5~10 A g^{-1}, verifies the high rate capability, which is especially significant for energy storage and delivery at high operation current densities. Fig. 6e compares the rate capabilities of PCM and a-PCMs supercapacitors at various current densities, the C_s retentions are 73.1 %, 87.1 %, 88.7 %, 88.8 % and 90.7 %, respectively for PCM, a-PCM$_{600}$, a-PCM$_{700}$, a-PCM$_{800}$ and a-PCM$_{900}$, showing the high rate capabilities of all supercapacitors. The highest rate capability of a-PCM$_{900}$ is mainly derived from the following factors: (1) the high electrons and ions conductivities owing to the relatively higher crystallinity and the higher fraction of mesopores decrease the inner resistance of electrode, ensuring a high rate capability; (2) the doped graphitic nitrogen by substitution of carbon atoms in graphite lattice offers extra conductivity; (3) the high hydrophilicity owing to the oxygen and nitrogen containing groups and rough surface by activation are beneficial for high electrode/electrolyte interfacial compatability and allow efficient electrolyte ions accumulation onto electrode even at high operation currents.

Cycling stability of supercapacitors were shown in Fig. 6f, C_s of a-PCM$_{900}$ supercapacitor decreases from 273.2 to 264.2 F g^{-1} after 1000 successive charging-discharging cycles at 1 A g^{-1}, the 96.7 % retaining ratio of its initial capacitance indicates the high cycling stability. Similarly, other a-PCMs and PCM also exhibit high cycling stability, suggests that the robust texture of beer derived porous carbons can endure the volumetric effect during the charging-discharging cycles. To sum up, due to the highest C_s, excellent rate capability and cycling stability, a-PCM$_{900}$ herein is the most preferential candidate as supercapacitor electrode.

To further understand the resistance and electrolyte diffusion kinetics of a-PCMs, EIS of PCM and a-PCMs supercapacitors were measured and compared. From Fig. 7a, Nyquist plots of all supercapacitors comprise a straight line at low frequency end and an arc at high frequency region. The intercept on real axis is the series resistance (R_s), which is the sum of electrolyte resistance, intrinsic active material resistance and the contact resistance between active material and collector,[58,59] R_s of a-PCM$_{900}$ capacitor is estimated to be 2.4 Ω, which is slightly lower than that of other devices (3.9, 3.1, 2.8, 2.7 Ω, for PCM, a-PCM$_{600}$, a-PCM$_{700}$, a-PCM$_{800}$ respectively). The similar R_ss are mainly due to narrow difference in conductivity due to the same fraction of conductive carbon black in electrodes and the same ionic conductivity of electrolyte. The arc at high-medium frequency region corresponds to the charge transfer resistance (R_{ct}), the arc diameters of a-PCMs supercapacitors are much smaller than that of PCM device, suggesting the more efficient electrolyte ions diffusion and accumulation on active materials owing to the high hydrophilicity, the higher surface area, as well as the efficient redox transformation of pseudo-capacitive nitrogen and oxygen containing groups at electrode-electrolyte interface. R_{ct} of PCM and a-PCM$_{600}$, a-PCM$_{700}$, a-PCM$_{800}$ and a-PCM$_{900}$ are 7.9, 2.9, 2.4, 1.3, and 1.2 Ω, respectively. The lowest R_{ct} of a-PCM$_{900}$ means the most efficient redox reaction at electrode-electrolyte interface and the rapid accumulation of electrolyte ions onto electrode surface,[58,59] which results in the highest EDL and pseudo-capacitance. At low frequency end, all supercapacitors show a straight line, the tail with a slope of 45 ° represents the Warburg diffusion resistance (Z_w), the much shorter distance of this diffusion section for a-PCMs capacitors suggests the much lower electrolyte ions diffusion resistances owing to the hollow textures containing both micropores and mesopores, as well as the high hydrophilicity. The almost vertical line of a-PCMs supercapacitors at low frequency end suggests the nearly ideal EDL capacitive behavior due to the substantially higher surface area by activation treatment. Considering the low R_s, R_{ct}, and Z_w, excellent capacitive performance can be achieved using a-PCMs as electrode materials. Fig. 7b displays the Bode plots of different supercapacitors, the phase angles of a-PCMs capacitors approach to -90 ° at low frequency, which means the ideal capacitive behavior. At the phase angle of -45 °, a-PCMs supercapacitors demonstrate more drastic frequency responses, suggesting the lower Z_w owing to the large and accessible surface areas, which are further beneficial for a higher rate capability. The response frequencies at -45 ° (f_0) for a-PCM$_{600}$, a-PCM$_{700}$, a-PCM$_{800}$ and a-PCM$_{900}$ are 0.326, 0.45, 0.53 and 0.58 Hz, respectively, all of which are higher over PCM supercapacitor (0.163 Hz). The response time (τ) based on the frequency at phase angle of -45°, at where the capacitive and resistive impedances are equal according to $\tau=1/f_0$,[52,60] are estimated to be 6.1, 3.0, 2.2, 1.9 and 1.7 s for PCM, a-PCM$_{600}$, a-PCM$_{700}$, a-PCM$_{800}$ and a-PCM$_{900}$ supercapacitors, the shortest response time for a-PCM$_{900}$ capacitor is mainly due to the lowest R_{ct}. All these electrochemical parameters validate that a-PCM$_{900}$ is the most promising electrode material in capacitive energy storage and delivery.

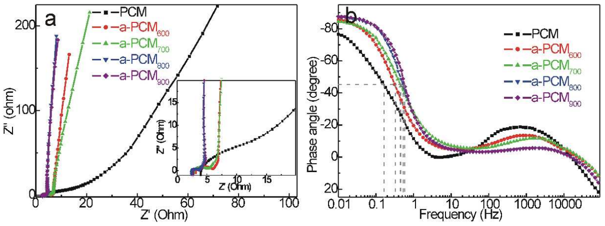

Fig. 7 (a) Nyquist plots of PCM and a-PCMs supercapacitors, inset: enlarged plots at high frequency region. (b) Bode phase angle as a function of frequency from EIS spectra.

Catalytic properties of a-PCMs

The highly porous texture with large surface area, high

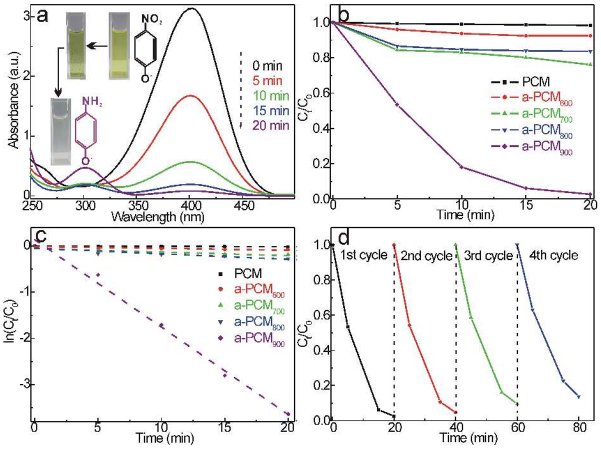

Fig. 8 (a) UV-vis absorption spectra during the catalytic reduction of 4-nitrophenol by a-PCM$_{900}$. Inset: digital images of solution before and after reduction. (b) C_t/C_0 and (c) $\ln(C_t/C_0)$ *vs* reaction time plots of solutions catalyzed by PCM, a-PCM$_{600}$, a-PCM$_{700}$, a-PCM$_{800}$, a-PCM$_{900}$. (d) Cycling stability of a-PCM$_{900}$.

hydrophilicity and the nitrogen containing structure make a-PCMs competitive candidates as catalysts toward certain reaction in aqueous media. To evaluate the catalytic activity of a-PCMs, the reduction of 4-nitrophenol by excess NaBH$_4$ was employed as a model reaction. Generally, this reaction can not occur in the absence of catalyst, the addition of NaBH$_4$ to 4-nitrophenol forms yellow 4-nitrophenolate ions featured by a strong absorption peak at 400 nm, which can be used to monitor the reaction extent.[23,61] From Fig. S9. PCM, a-PCM$_{600}$, a-PCM$_{700}$, and a-PCM$_{800}$ only show weak activity on reduction of 4-nitrophenol, which account for less than 20 % attenuation in absorbance within 20 min. In sharp contrast, the catalytic activity of a-PCM$_{900}$ is remarkably higher, the characteristic absorbance decreases apparently and almost fully vanishes within 20 min (Fig. 8a-b), which can also be intuitively visualized from the fading of yellow solution. Meanwhile, another peak at 300 nm belonging to 4-aminophenolate ions emerges and increases gradually, which to some extent excludes the adsorption of 4-nitrophenol onto a-PCM$_{900}$ and proves the catalytic reduction toward 4-aminophenol.[61,62] Given the much excessive NaBH$_4$ dosage, only 4-nitrophenol concentration can be considered in reaction kinetics fitting. From Fig. 8c, the plots of lnC_t/C_0 *vs* reaction time exhibit good linearity, suggesting the pseudo-first order reaction kinetics for catalytic reduction of 4-nitrophenol. The apparent rate constants (k), *viz* slopes of linear plots are -7.85×10^{-4}, -3.95×10^{-3}, -7.79×10^{-3}, -0.012, and -0.19 s^{-1}, respectively for PCM, a-PCM$_{600}$, a-PCM$_{700}$, a-PCM$_{800}$ and a-PCM$_{900}$, showing higher activation temperature is really beneficial for a higher catalytic activity. According to N 1s XPS analysis (inset in Fig. 5c), pyridinic-, pyrrolic-, and graphitic-N are included in carbon framework of a-PCM$_{900}$, all of these functionalities and the higher fraction of mesopores are beneficial for sufficient adsorption of 4-nitrophenic ions.[23] Moreover, the doped N serve as catalytically active sites *via* inducing the local high positive charge and spin density of adjacent carbon atoms and leading to the metal like catalytic activity.[23,63] Additionally, graphitic-N, accompanied with the graphitized carbon framework, are capable of enhancing the conductivity of a-PCM$_{900}$ and promoting the charge transfer at catalyst/4-nitrophenol interface. All of these factors converged in offering the high catalytic activity on 4-nitrophenol reduction.

The reusability of a-PCM$_{900}$ catalyst was also evaluated by 4 consecutive catalytic reaction cycles. The conversion of 4-nitrophenol maintains to be 86.3 % after 4 cycles, suggesting the high cycling stability of a-PCM$_{900}$. The catalyst after four cycles of catalytic reaction was examined by FTIR (Fig. S10), the absorptions belonging to 4-nitrophenol is undetectable in the catalyst, further confirms that the decreased absorbance at 400 nm (Fig. 8a) is caused by the reduction of 4-nitrophenol rather than adsorption. The decay in conversion ratio is mainly caused by the inevitable loss of catalyst during the sampling and rinse steps. In all, the high catalytic activity and well reusability render a-PCM$_{900}$ a promising noble metal free catalyst for 4-nitrophenol reduction.

Conclusions

The present work involves the simultaneous preparation of NCQDs and PCM *via* a facile and green hydrothermal strategy using beer as precursor. The as-obtained NCQDs show strong PL performance in solution and dry state, as well as robust anti-interference in complicate chemical media, highlighting the potential as an efficient fluorescent dye. The N containing PCM also shows great potential in supercapacitor electrodes and nonmetal catalyst. ZnCl$_2$ activation treatment at 900 °C dramatically enhances the capacitive performance as supercapacitor electrodes and catalytic activity on 4-nitrophenol reduction. These fluorescent, capacitive and catalytic carbon materials verify the great potential of beer in carbon materials fabrication.

Acknowledgements

This work was supported by NSFC (Nos. 61204078, U1304505, 61176004), Program for Innovative Research Team (in Science and Technology) in University of Henan Province (No. 13IRTSTHN026), Key Project of Science and Technology of Henan Province (No. 122102210561), Program for Changjiang Scholars and Innovative Research Team in University and the Key Project of Science and Technology of Xinxiang City.

Notes and references

School of Chemistry and Chemical Engineering, Collaborative Innovation Center of Henan Province for Green Manufacturing of Fine Chemicals, Key Laboratory of Green Chemical Media and Reactions, Ministry of Education, Henan Normal University, Xinxiang, 453007, China. E-mail: kjiang512@163.com

1 V. Sgobba and D.M. Guldi, *Chem. Soc. Rev.*, 2009, **38**, 165–184.
2 M. Burghard, H. Klauk and K. Kern, *Adv. Mater.*, 2009, **21**, 2586–2600.
3 X.J. Zhou, J.L. Qiao, L. Yang and J.J. Zhang, *Adv. Energy Mater.*, 2014, **4**, 1301523.
4 J.D. Fowler, M.J. Allen,V.C. Tung,Y. Yang, RB. Kaner and B.H. Weiller, *ACS Nano*, 2009, **3**, 301–306.
5 R.G. Mendes, A. Bachmatiuk, B. Büchner, G. Cuniberti and M.H. Rümmeli, *J. Mater. Chem. B*, 2013, **1**, 401–428.
6 S.L. Candelaria, Y.Y. Shao, W. Zhou, X.L. Li, J. Xiao, J.G. Zhang, Y. Wang, J. Liu, J.H. Li and G.Z. Cao, *Nano Energy*, 2012, **1**, 195–220.
7 L.M. Dai, D.W. Chang, J.B. Baek and W. Lu, *Small*, 2012, **8**, 1130–1166.
8 S.N. Baker and G.A. Baker, *Angew. Chem. Int. Ed.*, 2010, **49**, 6726–6744.
9 Y.P. Sun, B. Zhou, Y. Lin, W. Wang, K.A.S. Fernando, P. Pathak, M.J. Meziani, B.A. Harruff, X. Wang, H.F. Wang, P.G. Luo, H. Yang, M.E. Kose, B.L. Chen, L.M. Veca and S.Y. Xie, *J. Am. Chem. Soc.*, 2006, **128**, 7756–7757.
10 P.G. Luo, S. Sahu, S.T. Yang, S.K. Sonkar, J.P. Wang, H.F. Wang, G.E. LeCroy, L. Cao and Y.P. Sun, *J. Mater. Chem. B*, 2013, **1**, 2116–2127.
11 H.T. Li, Z.H. Kang, Y. Liu and S.T. Lee, *J. Mater. Chem.*, 2012, **22**, 24230–24253.
12 H.J. Yu, Y.F. Zhao, C. Zhou, L. Shang, Y. Peng, Y.H. Cao, L.Z. Wu, C.H. Tung and T.R. Zhang, *J. Mater. Chem. A*, 2014, **2**, 3344–3351.
13 W.B. Lu, X.Y. Qin, S. Liu, G.H. Chang, Y.W. Zhang, Y.L. Luo, A.M. Asiri, A.O. Al-Youbi and X.P. Sun, *Anal. Chem.*, 2012, **84**, 5351–5357.
14 C.Q. Ding, A.W. Zhu and Y. Tian, *Acc. Chem. Res.*, 2014, **47**, 20–30.
15 P. Roy, A.P. Periasamy, C. Chuang, Y.-R. Liou, Y.-F. Chen, J. Joly, C.T. Liang and H.T. Chang, *New J. Chem.*, 2014, **38**, 4946–4951.
16 C.X. Li, C. Yu, C.F. Wang and S. Chen, *J. Mater. Sci.*, 2013, **48**, 6307–6311.
17 Y.Q. Dong, H.C. Pang, H.B. Yang, C.X. Guo, J.W. Shao, Y.W. Chi, C.M. Li and T. Yu, *Angew. Chem. Int. Ed.*, 2013, **52**, 7800–7804.
18 Z.S. Qian, J.J. Ma, X.Y. Shan, H. Feng, L.X. Shao and J.R. Chen, *Chem. Eur. J.*, 2014, **20**, 2254–2263.
19 J.P. Paraknowitsch and A. Thomas, *Energy Environ. Sci.*, 2013, **6**, 2839–2855.
20 Y.S. Yun, C. Im, H.H. Park, I. Hwang, Y. Tak and H.J. Jin, *J. Power Sources*, 2013, **234**, 285–291.
21 Y.M. Tan, C.F. Xu, G.X. Chen, Z.H. Liu, M. Ma, Q.J. Xie, N.F. Zheng and S.Z. Yao, *ACS Appl. Mater. Interf.*, 2013, **5**, 2241–2248.
22 U.B. Nasini, V.G. Bairi, S.K. Ramasahayam, S.E. Bourdo, T. Viswanathan and A.U. Shaikh, *J. Power Sources*, 2014, **250**, 257–265.
23 X.K. Kong, Z.Y. Sun, M. Chen, C.L. Chen and Q.W. Chen, *Energy*

Environ. Sci., 2013, **6**, 3260–3266.

24 H. Q. Sun, Y.X. Wang, S.Z. Liu, L. Ge, L. Wang, Z.H. Zhu and S.B. Wang, *Chem. Commun*., 2013, **49**, 9914–9916.

25 S. Sahu, B. Behera, T.K. Maitib and S. Mohapatra, *Chem. Commun*., 2012, **48**, 8835–8837.

26 V.N. Mehta, S. Jha and S.K.r Kailasa, *Mater. Sci. Eng. C*, 2014, **38**, 20–27.

27 H.L. Wang, Z.W. Xu, A. Kohandehghan, Z. Li, K. Cui, X.H. Tan, T.J. Stephenson, C.K. King'ondu, C.M.B. Holt, B.C. Olsen, J.K. Tak, D. Harfield, A.O. Anyia and D. Mitlin, *ACS Nano*, 2013, 7, 5131-5141.

28 N. Brun, P. Osiceanu and M.M. Titirici, *ChemSusChem*, 2014, **7**, 397-401.

29 D.S. Dhawale, G.P. Mane, S. Joseph, C. Anand, K. Ariga and A. Vinu, *ChemPhysChem*, 2013, **14**, 1563–1569.

30 G. Nam, J. Park, S.T. Kim, D.B. Shin, N. Park, Y. Kim, J.S. Lee and J. Cho, *Nano Lett*., 2014, **14**, 1870-1876.

31 Y.H. Yang, J.H. Cui, M.T. Zheng, C.F. Hu, S.Z. Tan, Y. Xiao, Q. Yang and Y.L. Liu, ***Chem. Commun.*,** 2012, **48**, 380–382.

32 X.D. He, H.T. Li, Y. Liu, H. Huang, Z.H. Kang and S.T. Lee, *Colloids and Surfaces B*, 2011, **87**, 326–332.

33 Z.C. Yang, M. Wang, A.M. Yong, S.Y. Wong, X.H. Zhang, H. Tan, A.Y. Chang, X. Li and J. Wang, *Chem. Commun*., 2011, **47**, 11615–11617.

34 L.B. Tang, R.B. Ji, X.M. Li, K.S. Teng and S.P. Lau, *Part. Part. Syst. Charact*., 2013, **30**, 523–531.

35 S. Sahu, B. Behera, T.K. Maiti and S. Mohapatra, *Chem. Commun*., 2012, **48**, 8835–8837.

36 Y.P. Hu, J. Yang, J.W. Tian, L. Jia and J.S. Yu, *Carbon*, 2014, **77**, 775–782.

37 D. Sun, R. Ban, P.H. Zhang, G.H. Wu, J.R. Zhang and J.J. Zhu, *Carbon*, 2013, **64**, 424–434.

38 H. Ding, J.S. Wei and H.M. Xiong, *Nanoscale*, 2014, **6**, 13817–13823.

39 M.B. Wu, Y. Wang, W.T. Wu, C. Hu, X.N. Wang, J.T. Zheng, Z.T. Li, B. Jiang and J.S. Qiu, *Carbon*, 2014, **78**, 480–489.

40 Z.Y. Gao, F. Wang, J.L. Chang, D.P. Wu, X.R. Wang, X. Wang, F. Xu, S.Y. Gao and K. Jiang, *Electrochim. Acta*, 2014, **133**, 325–334.

41 M. Li, S.K. Cushing, X. Zhou, S. Guo and N. Wu, *J. Mater. Chem*., 2012, **22**, 23374–23379.

42 W. Li, Z.H. Zhang, B. Kong, S.S. Feng, J.X. Wang, L.Z. Wang, J.P. Yang, F. Zhang, P.Y. Wu and D.Y. Zhao, *Angew. Chem. Int. Ed*., 2013, **52**, 8151–8155.

43 S.J. Zhu, J.H. Zhang, S.J. Tang, C.Y. Qiao, L. Wang, H.Y. Wang, X. Liu, B. Li, Y.F. Li, W.L. Yu, X.F. Wang, H.C. Sun and B. Yang, *Adv. Funct. Mater*., 2012, **22**, 4732–4740.

44 S. Yorgun, N. Vural and H. Demiral, *Micropor. Mesopor. Mater*., 2009, **122**, 189–194.

45 T.H. Liou, *Chem. Eng. J*., 2010, **158**, 129–142.

46 Y.W. Zhu, S. Murali, M.D. Stoller, K.J. Ganesh, W.W. Cai, P.J. Ferreira, A. Pirkle, R.M. Wallace, K.A. Cychosz, M. Thommes, D. Su, E.A. Stach and R.S. Ruoff, *Science*, 2011, **332**, 1537–1541.

47 J. Jiang, Y. He, S. Li and H. Cui. *Chem. Commun*., 2012, **48**, 9634–9636.

48 F.Q. Zhang, Y. Meng, D. Gu, Y. Yan, Z.X. Chen, B. Tu and D.Y. Zhao, *Chem. Mater*., 2006, **18**, 5279–5288.

49 K. Mohanty, M. Jha, B.C. Meikap and M.N. Biswas, *Ind. Eng. Chem. Res*., 2005, **44**, 4128–4138.

50 Z. Burton and B. Bhushan, *Nano Lett*., 2005, **5**, 1607–1613.

51 T.E. Rufford, D. Hulicova-Jurcakova, Z.-H. Zhu and G.-Q. Lu. *Electrochem. Commun*., 2008, **10**, 1594–1597.

52 D.W. Wang, Y.G. Min, Y.H. Yu and B. Peng, *J. Colloid Interf. Sci*., 2014, **417**, 270–277.

53 C. Ma, Y.J. Li, J.L. Shi, Y. Song and L. Liu, Chem. Eng. J. 2014, **249**, 216–225.

54 X.T. Hong, K.S. Hui, Z. Zeng, K.N. Hui, L.J. Zhang, M.Y. Mo and M. Li, *Electrochim. Acta* 2014, **130**, 464–469.

55 Z. Ling, G. Wang, M.D. Zhang, X.M. Fan, C. Yu, J. Yang, N. Xiao and J.S. Qiu, *Nanoscale*, 2015, **7**, 5120–5125

56 H.X. Luo, Z.Y. Liu, L.M. Chao, X.C. Wu, X.D. Lei, Z. Chang. and X.M. Sun, J. Mater. Chem. A, 2015, **3**, 3667–3675.

57 S. Zhong, C.X. Zhan and D.P. Cao, *Carbon* 2015, **85**, 51–59.

58 L. Sun, C.G. Tian, Y. Fu, Y. Yang, J. Yin, L. Wang and H.G. Fu, *Chem. Eur. J*., 2014, **20**, 564–574.

59 D. Puthusseri, V. Aravindan, S. Madhavi and S. Ogale, *Energy Environ. Sci*., 2014, **7**, 728–735.

60 Z.S. Wu, K. Parvez, X.L. Feng and K. Müllen, *Nat. Commun*., 2013, **4**, 2487.

61 Y.F. Qiu, Z. Ma and P.A. Hu, *J. Mater. Chem. A*, 2014, **2**, 13471–13478.

62 X.L. Fang, J. Zang, X.L. Wang, M.S. Zheng and N.F. Zheng, *J. Mater. Chem. A*, 2014, **2**, 6191–6197.

63 Y.J. Gao, G. Hu, J. Zhong, Z.J. Shi, Y.S. Zhu, D.S. Su, J.G. Wang, X.H. Bao and D. Ma, *Angew. Chem. Int. Ed*., 2013, **52**, 2109–2113.